Synthesis, Structure, and Magnetic Properties of the Layered Bismuth Transition Metal Oxide Solid Solution $Bi_2Fe_{4-x}Ga_xO_9$

D. M. GIAQUINTA, G. C. PAPAEFTHYMIOU, W. M. DAVIS, AND H.-C. ZUR LOYE*

Department of Chemistry, Massachusetts Institute of Technology and the Francis Bitter National Magnet Laboratory, Cambridge, Massachusetts 02139

The solid solution $Bi_2Fe_{4-x}Ga_xO_9$ ($0 \leq x \leq 4$) was synthesized and investigated by X-ray diffraction, Mössbauer spectroscopy, and susceptibility measurements. The system was found essentially to follow Vegard's law. The crystal structure of the $x = 2$ member, $Bi_2Fe_2Ga_2O_9$, was solved. The structure is orthorhombic with space group *Pbam* (No. 55), $a = 7.946(1)$ Å, $b = 8.355(1)$ Å, and $c = 5.929(1)$ Å. Iron and gallium were nonstatistically distributed over two octahedral and two tetrahedral sites. The iron displayed a 60% preference for the octahedral positions. Magnetic susceptibility and Mössbauer measurements showed antiferromagnetic behavior. The ordering temperature, T_N, exhibited a strong dependence on x, decreasing rapidly with gallium doping from $T_N = 245 \pm 5$ K for $x = 0$ to $T_N < 4.2$ K for $x = 3$. Spin-glass-like behavior was observed in the gallium-substituted compounds, and a previously undetected spin rearrangement at 220 K for the $x = 0$ compound is reported. © 1992 Academic Press, Inc.

Introduction

Layered bismuth transition metal oxides (LBTMO), such as the Aurivillius phases (1–3) and several high T_c superconductors (4–9), have attracted attention in the recent literature because of their electronic and magnetic properties. The Aurivillius phases are a family of ferroelectrics (10–12) with the potential for superconductivity (13), while a number of layered bismuth copper oxides and the related thallium compounds exhibit superconductivity with transition temperatures as high a 125 K (4, 14).

The LBTMO are of interest not only because of the novelty of superconductivity, but because of their unique and complex magnetic behavior (15, 16), often caused by structural and magnetic two-dimensionality. The size difference between bismuth and the first row transition metals often promotes segregation of bismuth atoms from the transition metals within a given structure via the formation of Bi–O sheets that separate transition metal oxide motifs, such as the perovskitic regions in the Aurivillius compounds and planar regions in a number of bismuth transition metal oxides. This structural segregation can create pseudo-two-dimensional structures and consequently effect interesting properties that are often two-dimensional in nature.

One such family of LBTMO, $Bi_2M_4O_9$ (M = Fe, Mn, Al, and Ga (17–20)), which

* To whom correspondence should be addressed.

contains bismuth oxide planes that sandwich a metal oxide region consisting of two cation coordination sites, has been investigated in our laboratory. These compounds, in which octahedral and tetrahedral sites can accept both transition and main group metals, exhibit interesting and complex magnetic properties. We are in the process of studying the magnetic interactions that arise via a superexchange mechanism which couples the octahedral and tetrahedral sites. A systematic examination of $Bi_2M_{4-x}M'_xO_9$-type solid solutions is underway in order to elucidate how the metal–metal interactions effect the observed complex magnetic behavior, as well as to ascertain if the observed magnetic properties can be systematically altered via elemental substitutions.

The metal oxide region in the $Bi_2Fe_{4-x}Ga_xO_9$ structure containing the octahedral and tetrahedral sites is related structurally to the solid solution, $Ga_{2-x}Fe_xO_3$ ($0 \le x \le 1.6$) (21). The structure of $Ga_{2-x}Fe_xO_3$ is a 3D array consisting of two octahedrally and two tetrahedrally coordinated metal atoms (21–23). Although the transition metal regions in these two structures are related, the Bi–O sheets in $Bi_2M_4O_9$ create an essentially two-dimensional structure. It is therefore of interest to make comparisons between the electronic and magnetic properties of the solid solutions, $Bi_2Fe_{4-x}Ga_xO_9$, which has not been investigated, and $Ga_{2-x}Fe_xO_3$, which has been studied extensively since the first structural and magnetic characteristics were reported in 1960 (21, 24).

In this paper we describe the structure, magnetic properties and Mössbauer spectra of the solid solution $Bi_2Fe_{4-x}Ga_xO_9$, ($0 \le x \le 4$). This solid solution was investigated in order to determine the magnetic and structural effects of doping nonmagnetic Ga^{+3} into the layered bismuth transition metal oxide $Bi_2Fe_4O_9$. An unusual spin reorientation in $Bi_2Fe_4O_9$, discovered in the temperature-dependent Mössbauer study, is also discussed.

Experimental

Sample Preparation

Well-formed single crystals of the solid solution $Bi_2Fe_{4-x}Ga_xO_9$ with integral values of x were grown from a 5-g charge of a Bi_2O_3 flux using a fivefold excess of Bi_2O_3 (ÆSAR, 99.9%) and stoichiometric ratios of Fe_2O_3 (Cerac 99.99%) and Ga_2O_3 (Cerac, 99.99%) in a platinum crucible. While the use of alumina crucibles often resulted in aluminum contamination of the crystals, no platinum contamination was ever detected. The flux was heated to 950°C, soaked for 12 hr, slow cooled to 700°C at a rate of 5° per hour, and then rapidly cooled to room temperature. The flux was washed with dilute nitric acid and crystals smaller than 0.1 mm with an orthorhombic habit were separated from the flux matrix using a dissecting probe. The crystals grew as small brown prisms. Crystal stoichiometries were determined using a JEOL 733 wavelength dispersive microprobe.

Crystallographic Studies

Crystallographic data are summarized in Table I. Single-crystal diffraction studies of the $x = 2$ member, $Bi_2Fe_2Ga_2O_9$, were performed on an Enraf–Nonius CAD-4 diffractometer with graphite monochromated $MoK\alpha$ radiation ($\lambda = 0.71069$ Å). Cell constants and an orientation matrix for data collection were obtained from a least-squares refinement using the setting angles of 25 carefully centered reflections in the range of $18.00 < 2\Theta < 24.00°$. Based on the systematic absences of $0kl : k \ne 2n$ and $h0l : h \ne 2n$, packing considerations, a statistical analysis of intensity distribution, and the successful solution and refinement of the structure, the space group was determined to be $Pbam$ (No. 55); the same space group is also found for $Bi_2Fe_4O_9$ and $Bi_2Ga_4O_9$ (18, 19). A total of 1046 reflections were collected. The intensities of three representative reflections which were measured after every 60 min

TABLE I

SUMMARY OF CRYSTALLOGRAPHIC DATA FOR $Bi_2Fe_2Ga_2O_9$

Empirical formula	$Bi_2Fe_2Ga_2O_9$
Formula weight	813.09
Crystal color, habit	Amber, prismatic
Crystal dimensions (mm)	$0.080 \times 0.030 \times 0.030$
Crystal system	Orthorhombic
Space group	*Pbam* (No. 55)
No. reflections used for unit cell determination (2Θ range)	25 (18.0–24.0°)
Omega scan peak width at half height	0.32
Lattice parameters (Å)	
a	7.946 (1)
b	8.335 (1)
c	5.929 (1)
Volume ($Å^3$)	392.7
Z	2
D_{calc} (g/cm^3)	6.876
F_{000}	704
μ(Mo Kα) (cm^{-1})	549.16
Diffractometer	Enraf–Nonius CAD-4
Radiation	MoKα (λ = 0.71069 Å)
Temperature (°C)	24
Attenuator	Zr foil (factor = 17.9)
Scan type	ω
$2\Theta_{max}$	69.9°
No. of reflections measured	1046
No. observations ($I > 3.00 \sigma(I)$)	555
No. variables	24
Corrections	Lorentz-polarization Absorption (trans. factors: 0.87–1.29) Secondary extinction (coefficient: 0.74117E-06)
Residuals: R; R_w	0.053; 0.063
Goodness of fit indicator	2.15
Maximum peak in final diff. map	4.19 e$^-$/Å^3

of X-ray exposure time remained constant throughout data collection, indicating crystal and electronic stability. Data were corrected for Lorentz, polarization, absorption (25), and secondary extinction. Data were further corrected for absorption empirically (26).

All calculations were carried out on a MicroVAX 3500 with the use of TEXSAN crystallographic software (27). The structure was solved by direct methods (28). Refinement was performed using a full-matrix

least-squares calculation. The final values of the discrepancy factors were R = 0.053 (R = $\Sigma||F_o| - |F_c||/\Sigma|F_o|$ = 0.053) and R_w = 0.063 (R_w = $[(\Sigma w(|F_o| - |F_c|)^2/\Sigma wF_o^2)]^{1/2}$ = 0.063), w = $4F_o^2/\sigma^2(F_o^2)$. The goodness of fit was 2.15 and the highest peak in the final difference map was 4.19 e$^-$/Å^3. The atomic scattering factors were those of Cromer and Waber (25) and corrections for anomalous dispersions were from Cromer (29).

Precession photos of the other solid solution members were obtained on an En-

raf–Nonius Diffractis 581 X-ray generator equipped with a Charles Supper Co. precession camera using a precession angle of 10° and a film to crystal distance of 59 mm. Stoichiometry was verified using a JEOL 733 wavelength dispersive microprobe with EDS capabilities.

Polycrystalline Samples

Polycrystalline samples of the solid solution Bi$_2$Fe$_{4-x}$Ga$_x$O$_9$ were prepared in increments of 0.1 for values of $x = 0$ to 1 and in increments of 0.25 for values of $x = 1$ to 4. Stoichiometric amounts of the oxides Bi$_2$O$_3$ (ÆSAR, 99.9%), Fe$_2$O$_3$ (Cerac 99.99%), and Ga$_2$O$_3$ (Cerac, 99.99%) were ground under acetone, pressed into pellets, and heated at 850°C in air for 2 weeks with frequent grindings. The pellets were heated in Al$_2$O$_3$ crucibles on platinum foil to prevent aluminum contamination. Polycrystalline samples were structurally characterized by powder X-ray diffraction on a Rigaku RU300 at 10 kW with Cu$K\alpha$ radiation ($\lambda = 1.54184$ Å). NBS mica (SRM 675) was used as a standard for accurate peak positions. Lattice parameters were determined using the LATICE least-squares program.

Magnetic Measurements

Magnetic data were collected using a Quantum Design MPMS SQUID magnetometer at temperatures ranging from 5 to 400 K and in applied fields ranging from 0.1 to 50 kG. A scan length of 6 cm was used and 20 measurements were performed over the scan length. A total of three scans were averaged for each data point. All data were corrected for the diamagnetic contribution of a Kel-F sample holder.

Mössbauer Spectroscopy

Mössbauer spectra of various gallium doping levels for $1 \leq x \leq 3$ were obtained using a conventional constant acceleration spectrometer. Sample temperatures in the

TABLE II

POSITIONAL AND ISOTROPIC EQUIVALENT THERMAL PARAMETERS

Atom	x	y	z	B(eq)
Bi	0.1761(1)	0.1734(1)	0	0.41(3)
Ga	0.3515(4)	0.3364(4)	$\frac{1}{2}$	0.44(5)
Ga*	$\frac{1}{2}$	0	0.2578(6)	0.42(4)
Fe	$\frac{1}{2}$	0	0.2578	0.4
Fe*	0.3515	0.3364	$\frac{1}{2}$	0.4
O(1)	$\frac{1}{2}$	$\frac{1}{2}$	$\frac{1}{2}$	1.9(6)
O(2)	0.365(2)	0.206(1)	0.240(3)	0.6(2)
O(3)	0.133(3)	0.405(2)	$\frac{1}{2}$	0.4(3)
O(4)	0.153(3)	0.429(2)	0	0.4(3)

range $4.2 \leq T \leq 300$ K were achieved by the use of a Janis Supervaritemp dewar and a Lake Shore temperature controller. The source was ^{57}Co(Rh) maintained at room temperature. Isomer shifts are reported relative to metallic iron at room temperature.

Results

Structural

A small well-formed amber crystal of Bi$_2$Fe$_2$Ga$_2$O$_9$ with the approximate dimensions 0.080 × 0.030 × 0.030 mm was used for the structure determination. The final positional and thermal parameters are listed in Table II. Selected interatomic bond distances are shown in Table III.

A view parallel to the ab-plane of Bi$_2$Fe$_2$Ga$_2$O$_9$ is shown in Fig. 1 (the bismuth–oxygen bonds have been omitted for clarity). The structure consists of columns of edge-sharing octahedra which are corner-shared with corner-sharing tetrahedra, as shown in Fig. 2. The octahedra are located in layers that are separated by doubly packed tetrahedral layers. These layers form slabs of alternating octahedral–tetrahedral–octahedral coordination. The slabs in turn are separated from each other by planes of bismuth and oxygen. The octahedra are connected across the tetrahedral and

TABLE III

INTRAMOLECULAR DISTANCES

Atom	Atom	Distance	Atom	Atom	Distance
Bi	O(2)	2.084(14)	Ga*	Ga*	2.873(8)
Bi	O(4)	2.141(20)	Ga*	Fe*	3.364(2)
Bi	O(4)	2.445(20)	Fe	O(2)	2.025(13)
Ga	O(1)	1.803(3)	Fe	O(3)	1.951(14)
Ga	O(2)	1.892(15)	Fe	O(4)	2.041(14)
Ga	O(3)	1.828(21)	Fe	Fe	2.873(8)
Ga	Ga*	3.364(4)	Fe	Fe*	3.364(2)
Ga*	O(2)	2.025(13)	Fe*	O(1)	1.803(3)
Ga*	O(3)	1.951(14)	Fe*	O(2)	1.892(15)
Ga*	O(4)	2.041(14)	Fe*	O(3)	1.828(21)

bismuth oxide layer via edge-sharing oxygens located in the tetrahedral and bismuth oxide plane, respectively. The octahedra are tetragonally distorted; the longest and shortest metal oxygen distances are to the edge-shared oxygens in the bismuth oxide and the tetrahedral plane, respectively. The metal–oxygen bond lengths in the slightly distorted tetrahedra vary from 1.80 to 1.89 Å, as shown in Table III. The shortest metal oxygen bond of the tetrahedra, 1.80 Å, is directed toward an oxygen which corner-shares two adjacent tetrahedra. In contrast, the bond to the oxygen which corner-shares one octahedron and one tetrahedron is the longest metal oxygen bond, 1.89 Å, which originates from a tetrahedron. The bismuth atoms are located at the apices of trigonal pyramids formed by mutually orthogonal, short (2.1 Å) Bi–O bonds. If the second-, and third-, nearest neighbors are included, the bismuth ions are surrounded by eight oxygens. All oxygens in the structure are tetrahedrally coordinated.

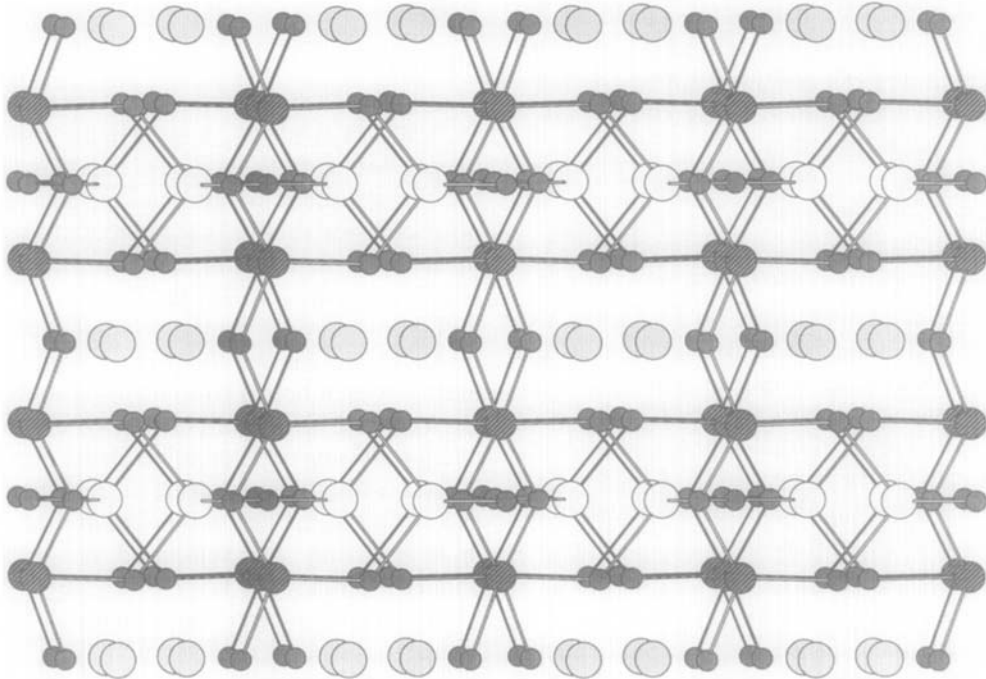A view perpendicular to the *ab*-plane, Fig. 3, shows a complicated packing net-

FIG. 1. The 2 × 2 × 2 unit cells of $Bi_2Fe_2Ga_2O_9$ viewed parallel to the *ab*-plane. Bismuth: ○; Iron: ●; Oxygen: ●; Gallium: ○.
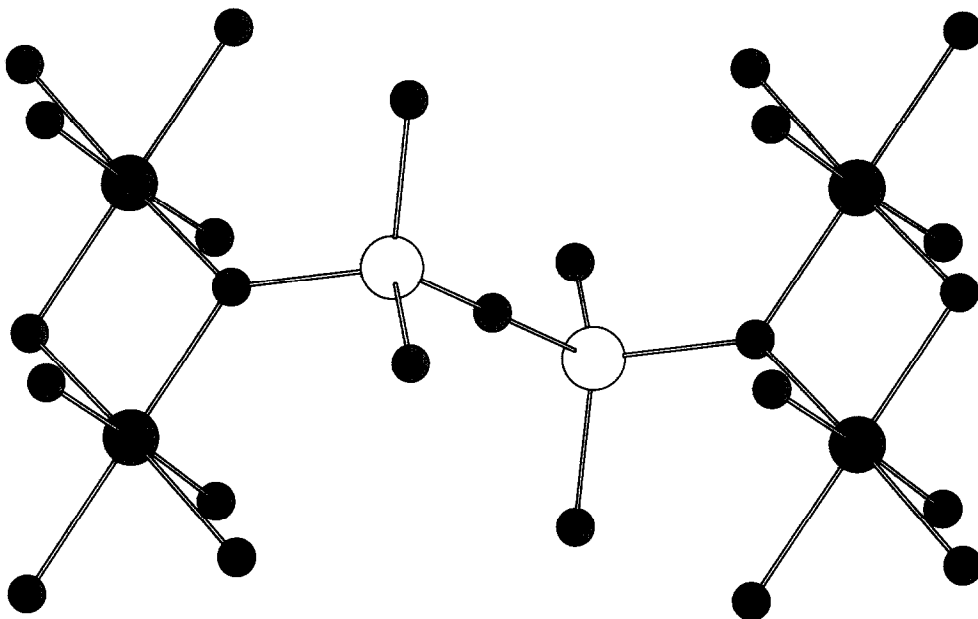
FIG. 2. A view of edge-shared octahedral and corner-shared tetrahedral cation coordination sites.

work of distorted fivefold symmetry. The fivefold rings are made up of corner-shared polygons in repeating groups of corner-shared tetrahedra, tetrahedra, octahedra, tetrahedra, octahedra. The order of planes going into the page is bismuth–octahedral sites–tetrahedral sites–octahedral sites–bismuth (the bismuth–oxygen bonds have been omitted for clarity).

In the structure the iron and gallium are nonstatistically distributed over the octahedral and tetrahedral sites. In comparison with the solid solution $Ga_{2-x}Fe_xO_3$, where the gallium sits exclusively on one tetrahedral site while the other somewhat distorted tetrahedron is randomly populated by both iron and gallium (22, 23), one might have expected either an ordered arrangement of gallium on the tetrahedral site or a statistical distribution of iron and gallium over the two sites. Refinement of the iron and gallium sites as stoichiometric positions (i.e., S.O.F. = 0.5/metal) resulted in divergence regardless of metal assignment. Conse-

quently, a mixed occupancy model was used and the occupancies of each site were refined with the restriction that total occupancy = 0.5. This refinement yielded a 60:40 distribution of iron:gallium on the octahedral sites. Mössbauer spectroscopy was used to independently determine and confirm the distribution of iron on the octahedral and tetrahedral sites. The refined population ratio of iron to gallium on the octahedral sites is 60:40, as determined by both Mössbauer spectroscopy (vide infra) and X-ray crystallography.

Lattice parameters for all members of the solid solution were determined from powder X-ray diffraction patterns. The powder pattern of $Bi_2Fe_4O_9$, Table IV, is virtually identical to that of the isostructural $Bi_2Ga_4O_9$. The powder patterns of all members of the solid solution $Bi_2Fe_{4-x}Ga_xO_9$ could therefore be readily indexed and their lattice parameters determined. The lattice parameters apparently follow Vegard's law across the range of x, as shown in Fig. 4. The slight
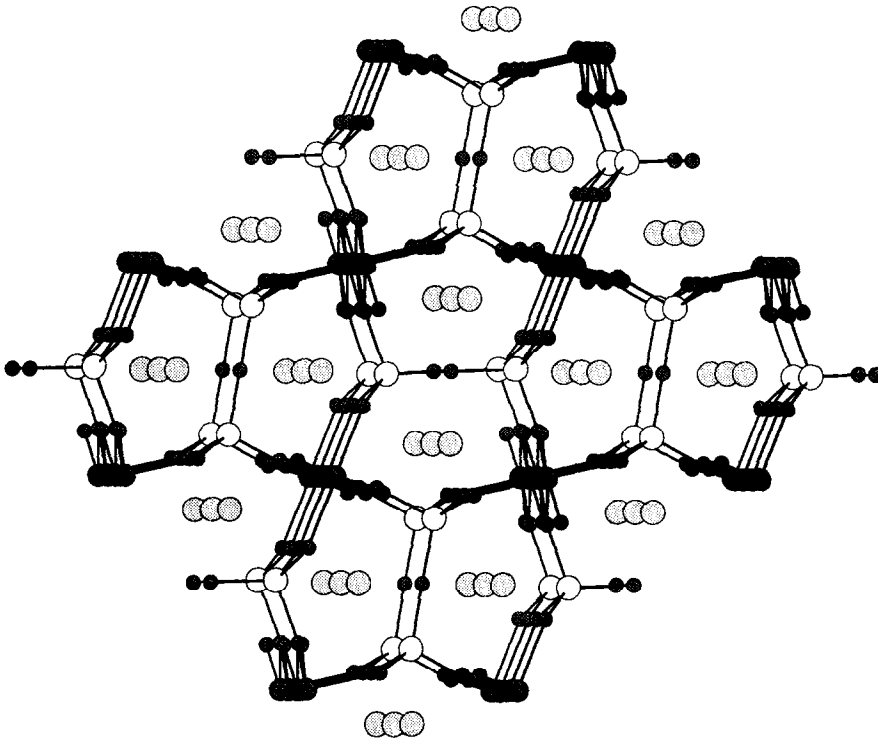
FIG. 3. A view of distorted fivefold nets perpendicular to the ab-plane. The order of planes going into the page is bismuth–octahedral sites–tetrahedral sites–octahedral sites–bismuth (the bismuth–oxygen bonds have been omitted for clarity).

deviation from ideal behavior, presumably, is due to the nonstatistical distribution of iron and gallium over the octahedral and tetrahedral sites. The compounds gradually changed color across the solid solution from $Bi_2Fe_4O_9$, red-brown, to $Bi_2Ga_4O_9$, yellow-white.

Magnetism

Magnetic measurements showed that the solid solution $Bi_2Fe_{4-x}Ga_xO_9$, for $0 \le x \le 2$ orders antiferromagnetically. This data is in agreement with the previously reported antiferromagnetic behavior of $Bi_2Fe_4O_9$ (*19*). The susceptibility plots display a very broad maximum, as shown for $Bi_2Fe_4O_9$ in Fig. 5a, which is often associated with either lower dimensional magnetic ordering (*30*) or

a second-order 3D magnetic phase transition (*31*). The Néel temperature, T_N, was determined to be the temperature of the point of inflection below the maximum (*31*). Using this method our T_N of 245 K agrees with the data published by Tutov *et al.* (*19*).

The change in the susceptibility data with gallium doping in $Bi_2Fe_{4-x}Ga_xO_9$ is shown in Figs. 5b and 5c for $Bi_2Fe_{3.7}Ga_{0.3}O_9$ and $Bi_2Fe_{3.1}Ga_{0.9}O_9$, respectively. The antiferromagnetic ordering temperature drops with gallium content and the shape of the susceptibility curve changes. In the susceptibility plot of $Bi_2Fe_{3.7}Ga_{0.3}O_9$ (Fig. 5b) one can observe a low temperature rise in magnetization due to uncompensated spins, which is not observed for larger gallium contents, as in $Bi_2Fe_{3.1}Ga_{0.9}O_9$ (Fig. 5c).

TABLE IV

X-RAY POWDER DATA[a] FOR $Bi_2Fe_4O_9$

d_{obs} (Å)	h	k	l	I/I_o
6.0479	0	0	1	25
4.2299	0	2	0	15
4.0044	2	0	0	10
3.7246	1	2	0	2
3.6143	2	1	0	2
3.1701	1	2	1	100
3.0920	2	1	1	85
2.8949	2	2	0	76
2.6652	1	3	0	48
2.5337	3	1	0	21
2.4390	0	2	2	12
2.3975	2	0	2	20
2.3073	2	1	2	21
2.0347	1	4	0	22
1.9317	3	3	0	50
1.8407	4	1	1	44

[a] Lattice positions were corrected with NBS mica (SRM 675).

The change in T_N with gallium doping in $Bi_2Fe_{4-x}Ga_xO_9$ is shown in Fig. 6. Small amounts of doping, up to $x = 0.2$, cause very little change in T_N. Additional gallium, $x = 0.2$ to 0.6, however, causes a precipitous drop in T_N from 230 to 60 K. Further addition of gallium, $x = 0.6$ to 3, causes T_N to drop slowly but steadily toward zero. In the region $x = 0.2$ to 0.6, where T_N changes by about 170 K, the susceptibility plots show characteristic second order antiferromagnetic behavior, with a broad maximum (32), followed by a rise in the magnetization due to uncompensated spins (Fig. 5b).

The susceptibility plots for the region of the solid solution, $x = 0.6$ to 3, where the transition temperatures are between 0 and 50 K, show well-behaved paramagnetic behavior up to the antiferromagnetic transition. The susceptibility below T_N, however, is very sensitive to changes in magnetic history; a field dependence and hysteresis is apparent, as shown in Fig. 7, for samples having $x \geq 0.6$. The type of magnetic behav-

ior observed when heating a sample from 5 K to room temperature depends on whether or not the initial cooling of the sample was performed in the presence or absence of a magnetic field. Loading a sample into the magnetometer with the applied field already on results in magnetic behavior that is ferromagnetic in appearance, while zero field produces behavior that is characteristic for an antiferromagnet. No field history dependent behavior is observed for samples with $0 \leq x \leq 0.5$.

Mössbauer

(a) $Bi_2Fe_4O_9$. Mössbauer spectra were collected between room temperature and 4.2 K. Representative spectra at selected temperatures are shown in Fig. 8. Mössbauer parameters derived from least-square fits of the experimental data to theoretical models are tabulated in Table V. At high temperatures, $T \geq 250$ K, the spectra are composed of the superposition of two well
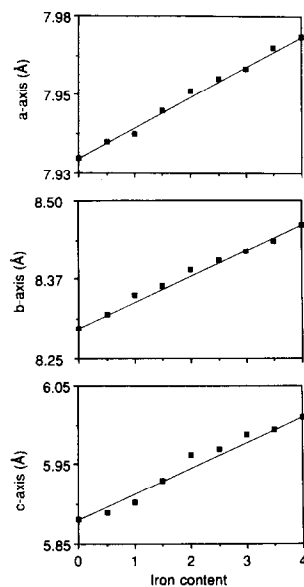

FIG. 4. Lattice parameters for the solid solution $Bi_2Fe_{4-x}Ga_xO_9$. The solid line represents change expected according to Vegard's law.
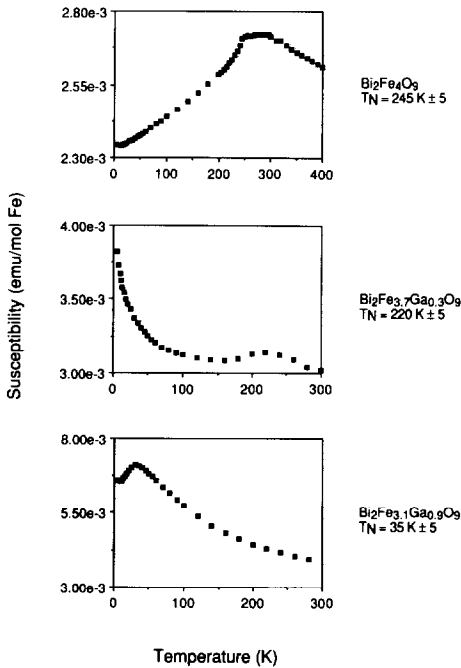
FIG. 5. Magnetic susceptibility (emu/mol Fe) of (a) $Bi_2Fe_4O_9$, (b) $Bi_2Fe_{3.7}Ga_{0.3}O_9$, and (c) $Bi_2Fe_{3.1}Ga_{0.9}O_9$ as a function of temperature (K). T_N (a) = 245 K ± 5, T_N (b) = 220 K ± 5, T_N (c) = 35 K ± 5.

resolved quadrupole doublets with isomer shifts and quadrupole splittings δ_1 = 0.19 mm/sec, ΔE_{Q1} = 0.78 mm/sec, and δ_2 = 0.48 mm/sec, ΔE_{Q2} = 0.54 mm/sec, consistent with high-spin Fe^{+3} ions at 250 K in tetrahedral and octahedral environments, respectively. The intensity ratio of the two
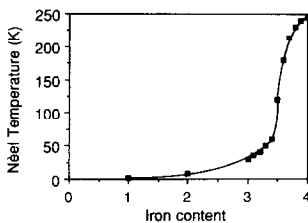

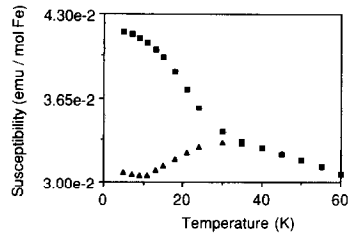FIG. 6. Transition temperature, T_N, of the solid solution $Bi_2Fe_{4-x}Ga_xO_9$ as a function of iron content. The solid line is added to guide the eye.

FIG. 7. Hysteresis effect from spin-glass-like behavior of $Bi_2Fe_{3.1}Ga_{0.9}O_9$. Cooling in the presence of a 40-kG field, ■, resulted in ferromagnetic-like behavior, while cooling in the absence of a field, ▲, resulted in antiferromagnetic behavior. T_N = 35 K ± 5.

signals is 1 : 1 in accordance with the crystallographic structure of the compound, which contains equal numbers of tetrahedral and octahedral sites. With decreasing temperature a complex magnetic behavior is observed within three distinct temperature regions. (see Fig. 8.)
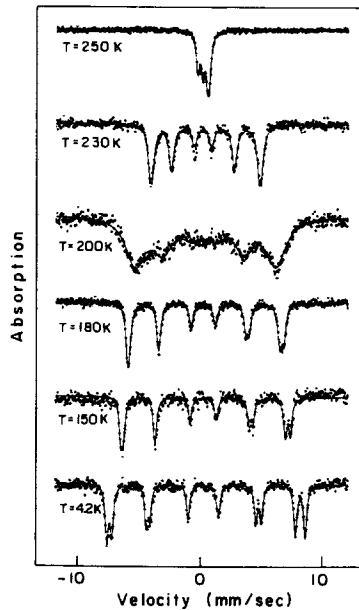

FIG. 8. Mössbauer spectra of $Bi_2Fe_4O_9$ at different temperatures. The solid line is the least-squares fit of the data to theoretical models with parameters given in Table V.

TABLE V

MÖSSBAUER PARAMETERS FOR THE SOLID SOLUTION $Bi_2Fe_{4-x}Ga_xO_9$

	T (K)	δ^a (mm/sec)	ΔE_Q or ε (mm/sec)	H_{hf} (kOe)	$\Gamma/2$ (mm/sec)	% Area	T_N (K)
$x = 0$	250	0.48^b	0.54	—	0.15	48	245
		0.19^c	0.78	—	0.15	52	
	230	0.34^d	0.225	277	0.27	100	
	200	0.38^d	0.18	358	0.95	100	
	150	0.45	0.15	432	0.14	42	
		0.34	0.16	412	0.18	58	
	4.2	0.48	0.15	505	0.16	50	
		0.34	0.16	467	0.17	50	
$x = 1$	80	0.50	0.54	—	0.17	55	40
		0.26	0.79	—	0.16	45	
	4.2	0.48	-0.01	484	0.27	42	
		0.37	0.07	442	0.40	58	
$x = 2$	80	0.53	-0.56	—	0.15	62	8
		0.24	0.80	—	0.14	38	
	4.2	0.49^d	—	437	0.59	100	
$x = 3$	80	0.50	0.57	—	0.16	69	<4.2
		0.24	0.80	—	0.12	31	
	4.2	0.50	0.60	—	0.25	62	
		0.24	0.86	—	0.22	38	

[a] Isomer shifts are reported relative to metallic iron at room temperature.
[b] Octahedral sites.
[c] Tetrahedral sites.
[d] Single, averaged site fits owing to unresolved octahedral and tetrahedral magnetic subsites.

The onset of magnetic hyperfine interactions occurs at $T_N = 245$ K $\pm$ 5 in agreement with our magnetic measurements. The functional dependence of the magnitude of the magnetic hyperfine field on the temperature is shown in Fig. 9. At $T = 220$ K a dramatic broadening of the Mössbauer spectra sets in. By $T = 180$ K, sharp 6-line magnetic spectra are recovered. With decrease in temperature, as the magnetization of the compound approaches saturation, two magnetic subcomponents which are associated with the octahedral and tetrahedral iron sites, become discernible. There is a slight difference in the local saturation magnetic moments between the two subsites that is reflected in the magnitudes of their saturated magnetic hyperfine fields of H_{sat}(oct) = 505 kOe and H_{sat}(tet) = 467 kOe at $T = 4.2$ K (Fig. 9).

With the exception of the anomalous spectral broadening at $T \sim 220$ K the overall magnetic behavior is consistent with a 3D antiferromagnetic phase transition. The observed anomalous broadening can be a result of a spin reorientation (33–35) toward a close-lying (in energy) different easy direction of magnetization. Another possibility is a structural phase transition, such as a second-order displacive transition.

The theoretical analysis of the Mössbauer spectra reveals that the quadrupolar interaction ε, a small perturbation to the dominant magnetic interaction below T_N, changes continuously from $\varepsilon = 0.225$ mm/sec for $T \geq 230$ K to $\varepsilon = 0.155$ mm/sec for $T \leq 150$ K (here an average between tetrahedral and octahedral sites is cited. See Table IV). For a magnetic phase transition, in the absence of a structural change
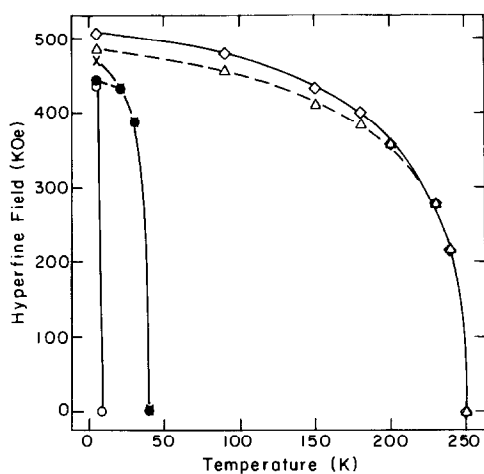
FIG. 9. Magnetic hyperfine field measured by Möss-bauer spectroscopy for the solid solution Bi_2Fe_{4-x} Ga_xO_9 as a function of temperature. $\diamond$: $Bi_2Fe_4O_9$ octahedral sites; $\triangle$: $Bi_2Fe_4O_9$ tetrahedral sites; X: Bi_2 Fe_3GaO_9 octahedral sites; ●: $Bi_2Fe_3GaO_9$ tetrahedral sites. Coincident points are the result of single, averaged site fits due to poorly resolved subsites. ○: Bi_2 $Fe_2Ga_2O_9$ average sites.

$$\varepsilon = \tfrac{1}{4} \Delta E_Q (3 \cos^2\theta - 1), \qquad (1)$$

where ΔE_Q is the quadrupole splitting above T_N and θ is the angle of the magnetic hyperfine field, H_{hf}, with respect to the principal component of the electric field gradient, V_{zz}, at a given crystallographic site. For $\Delta E_{Qave} = 0.66$ mm/sec between the octahedral and tetrahedral sites at $T = 250$ K, the change in ε observed would predict a spin reorientation of about $10°$ from $\theta° = 27°$ between H_{hf} and V_{zz} at $T > 200$ K to $\theta° = 37°$ for $T < 200$ K. Such a spin-reorientation process is certainly plausible given the structural complexity of the compound. Magnetic structure determination by neutron diffraction measurements (17) at 80 K has revealed a complex magnetic order with colinear antiferromagnetic pairs of moments defining three magnetic sublattices within the unit cell. However, if a structural phase transition has also taken place, Eq. (1) would not be applicable and no prediction

on $\theta°$ can be made. Nevertheless, the broadening of the Mössbauer spectra is consistent with spin fluctuations between easy directions of magnetization with a relaxation frequency close to the Larmor precession frequency, $\nu_L = (g_n\mu_n/\hbar)H_{hf} = 2.8 \times 10^7$ sec^{-1}, of the ^{57}Fe nuclear spin in the effective magnetic field of 358 kOe observed at $T = 200$ K.

(b) $Bi_2Fe_{4-x}Ga_xO_9$ solid solution. For low gallium doping the relative intensity of octahedral to tetrahedral quadrupole doublets observed above T_N indicate that there is no preferential ordering between the iron and the gallium. For higher gallium doping, however, the iron preferentially occupies the octahedral sites, with the octahedral to tetrahedral ratio of iron occupation being 2.225 at $x = 3$ and approaching 1 as x goes to zero, see Fig. 10.

The Mössbauer spectra for the gallium doped samples showed a rapidly decreasing T_N with increasing x (see Fig. 9) consistent with the magnetic measurements shown in Fig. 6. No anomalous spectral broadening was observed for these samples at any temperature. The temperature dependence of the normalized hyperfine
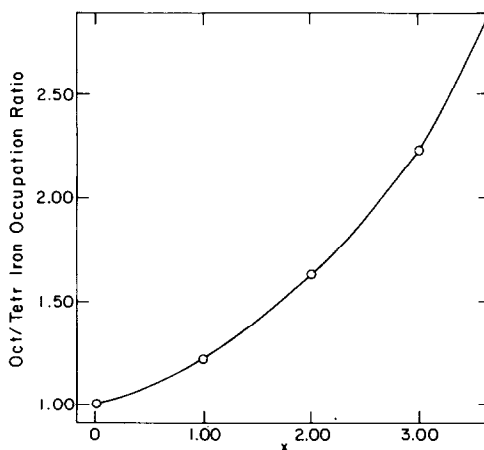

FIG. 10. Octahedral/tetrahedral occupation ratio for iron in $Bi_2Fe_{4-x}Ga_xO_9$ as a function of x.

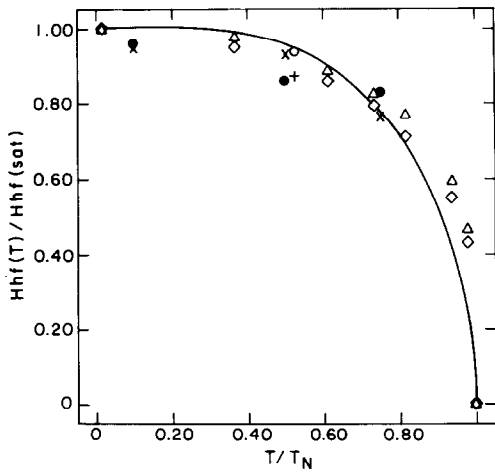FIG. 11. Normalized magnetic hyperfine field versus reduced temperature for Bi$_2$Fe$_{4-x}$Ga$_x$O$_9$. $\Diamond$: Bi$_2$Fe$_4$O$_9$ octahedral sites; $\triangle$: Bi$_2$Fe$_4$O$_9$ tetrahedral sites; X: Bi$_2$Fe$_3$GaO$_9$ octahedral sites; ●: Bi$_2$Fe$_3$GaO$_9$ tetrahedral sites; O: Bi$_2$Fe$_2$Ga$_2$O$_9$ average sites. The solid line is theoretical for the Brillouin function with $S = \frac{5}{2}$.

fields $H_{hf}(T)/H_{hf}(sat)$ are plotted vs. reduced temperature T/T_N in Fig. 11. Here we have assumed that saturation magnetic fields, similar to those of Bi$_2$Fe$_4$O$_9$, would have been obtained for the gallium-doped samples if low enough values of T could be achieved experimentally. Within this assumption, we observe that for values of x = 0, 1, and 2 the experimental data follow reasonably well an $S = \frac{5}{2}$ Brillouin function as expected for a 3D magnetic phase transition which can be described by the molecular field theory (31, 32). The degree of scattering away from the Brillouin function is not large enough to justify characterization of the transition as other than three dimensional.

Discussion

The values of T_N obtained from the Mössbauer study agree with those of the magnetic measurements. The broadness of the transition in the susceptibility plots might be interpreted as low-dimensional magnetic ordering, however, its shape is more akin to those due to three-dimensional, second-order transitions, which result in no discontinuity in the χ vs T plots at T_N (31, 32). This interpretation is supported by the Mössbauer data, discussed above, which is also consistent with a 3D magnetic phase transition.

Excellent agreement, also, was found between the octahedral to tetrahedral ratio of iron occupation as determined by Mössbauer spectroscopy and single-crystal X-ray diffraction, confirming that the cation distribution in both our single crystals and polycrystalline powders are the same. In a previous study (20) it was claimed that in crystals of Bi$_2$Fe$_2$Ga$_2$O$_9$, prepared by a laser melt technique, the gallium and iron atoms were preferentially ordered on tetrahedral and octahedral sites, respectively. This is in disagreement with both our Mössbauer and single-crystal diffraction data, and we can only speculate that due to the high temperatures and short reaction times (in comparison with slow crystallization from a flux) employed by the laser technique, preferential ordering occurs for kinetic reasons. This is an interesting possibility which we are presently exploring.

The effect of gallium doping on the transition temperature, T_N, in Bi$_2$Fe$_{4-x}$Ga$_x$O$_9$ shows a strong concentration dependence for x between 0.2 and 0.6, see Fig. 6, where T_N drops from 230 to 60 K. Rapid drops in the antiferromagnetic transition temperature for doping levels exceeding some small threshold value have been observed in other iron-containing oxides (36) and are characteristic of systems having competing magnetic interactions (37). In systems with noncompeting magnetic interactions the magnetic ordering temperature is gradually reduced with increasing dilution until, at the percolation limit, there is no longer any infinite cluster of atoms connected by magnetic interactions, and consequently long-range magnetic order ceases. In systems having competing magnetic interactions, on the other hand, the magnetic order

of the pure system breaks down more quickly with dilution and spin-glass phenomena can occur.

The breakdown in the magnetic order in $Bi_2Fe_{4-x}Ga_xO_9$ is not a simple percolation effect, as indicated by the rapid drop in T_N with gallium doping, but more likely a spin-frustration phenomenon, such as a spin-glass-like behavior, due to competing next-nearest neighbor exchange interactions. These interactions have the effect of destabilizing the magnetic long-range order produced by the nearest-neighbor exchange interactions. The effects of spin frustration are observed below the transition temperature in the magnetic susceptibility data, see Fig. 7, in the form of field and magnetic-history-dependent behavior, due to uncompensated spins created by the dilution of magnetic iron with nonmagnetic gallium.

These changes in the magnetic order are also noticeable in the Mössbauer data, where a change in the spin direction is observed as a function of gallium doping. Theoretical fits of the sample with composition $Bi_2Fe_3GaO_9$ result in a value of the quadrupolar perturbation ε close to zero, indicating that $\theta° \sim 54°$. This is quite different from the spin direction $\theta° \sim 37°$ in the all-iron composition, $Bi_2Fe_4O_9$. The magnetic structure in terms of the direction of the magnetization relative to the crystalline axes, therefore, depends on, and changes with, the degree of gallium doping. A new local magnetic order is established as an increasing number of nonmagnetic Ga^{+3} ions replace the magnetic Fe^{+3} ions in the crystal lattice, perhaps precipitating the sharp decline in T_N for $0.2 \leq x \leq 0.6$. This doping region may represent the regime in which the new local order is being established. For smaller doping levels, $0 \leq x \leq 0.2$, the system retains its long range magnetic order, with only a small decrease in the strength of the exchange interaction energy due to the introduction of nonmagnetic Ga^{+3} ions. For doping levels exceeding $x = 0.6$, only short-range magnetic interactions remain with a concomitant change in the Néel temperature that subsequently decreases to zero at the percolation limit as most of the Fe^{+3} has been replaced by Ga^{+3}. This loss of long range magnetic order in favor of only short-range order would result in a spin-glass type of magnetic structure, which is consistent with the observation of increasingly broader magnetic Mössbauer spectral widths of $\Gamma/2 = 0.16, 0.34$ and 0.59 for $x = 0, 1$, and 2, respectively. See Table V.

The spin reorientation in $Bi_2Fe_4O_9$ can be explained without invoking a structural change. In centrosymmetric structures it is possible to lose the inversion symmetry during a magnetic transition, such as antiferromagnetic ordering. In such cases the appearance of ferroelectricity and piezoelectricity is expected. In fact, according to Goshen *et al.* (*38*) magnetic symmetry changes brought on by antiferromagnetic ordering can induce ferroelectric transitions. This behavior has been predicted to occur in the isostructural $Bi_2Mn_4O_{10}$, and, if it did occur in $Bi_2Fe_4O_9$, could explain the broadening of the Mössbauer spectrum around 200 K.

It has been suggested based on neutron data on $Bi_2Fe_4O_9$ that at 4.2 K all the spins are aligned antiparallel within the plane of the transition metal slabs (*17*). The spin rearrangement that we have observed, therefore, indicates that above 220 K the spins are oriented in a different fashion. We are planning to carry out neutron diffraction measurements in order to ascertain the nature of this spin rearrangement, which could be due to a structural or magnetic transition in the material.

Conclusions

The complete solid solution Bi_2Fe_{4-x} Ga_xO_9 has been synthesized and investigated structurally and magnetically. The crystal structure of the $x = 2$ member, $Bi_2Fe_2Ga_2O_9$, was solved and determined to be

isostructural with the end members, Bi_2 Fe_4O_9 and $Bi_2Ga_4O_9$. Polycrystalline samples were seen essentially to follow Vegard's law. The doping of nonmagnetic Ga^{3+} for magnetic Fe^{3+} caused a precipitous drop in the antiferromagnetic transition temperature, T_N, and spin-glass-like behavior was observed by magnetic measurements and Mössbauer spectroscopy. A change in the spin direction and consequently the magnetic structure was also observed by Mössbauer spectroscopy as a result of gallium doping. A previously unreported spin rearrangement was discovered for the $x = 0$ sample.

Acknowledgments

References

1. B. AURIVILLIUS, Ark. Kemi 1, 463 (1949).
2. B. AURIVILLIUS, Ark. Kemi 1, 499 (1949).
3. B. AURIVILLIUS, Ark. Kemi 2, 519 (1950).
4. C. W. CHU, J. BECHTOLD, L. GAO, P. H. HOR, AND Z. J. HUANG, Phys. Rev. Lett. 60, 941 (1988).
5. M. FUKUHARA, A. S. BHALLA, L. N. MULAY, AND R. E. NEWNHAM, J. Mater. Res. 4, 273 (1989).
6. J. B. GOODENOUGH AND A. MANTHIRAM, J. Solid State Chem. 88, 115 (1990).
7. H. MÜLLER-BUSCHBAUM, Angew. Chem. 101, 1503 (1989).
8. B. RAVEAU, C. MICHEL, M. HERVIEU, D. GROULT, AND J. PROVOST, J. Solid State Chem. 85, 181 (1990).
9. A. W. SLEIGHT, Science 242, 1519 (1988).
10. B. AURIVILLIUS, Phys. Rev. 126, 893 (1962).
11. E. C. SUBBARAO, J. Phys. Chem. Solids 23, 665 (1962).
12. R. E. NEWNHAM, R. W. WOLFE, AND J. F. DORRIAN, Mater. Res. Bull. 6, 1029 (1971).
13. K. A. YEE, T. A. ALBRIGHT, D. JUNG, AND M. WHANGBO, Angew. Chem. Int. Ed. Engl. 28, 750 (1989).
14. H. MAEDA, Y. TANAKA, T. FUKUTOMI, AND T. ASANO, Jpn. J. Appl. Phys. 27, L209 (1988).
15. Y. LE PAGE, W. R. McKINNON, J.-M. TARASCON, AND P. BARBOUX, Phys. Rev. B 40, 6810 (1989).
16. J.-M. TARASCON et al., Phys. Rev. B 39, 11587 (1989).
17. N. SHAMIR, E. GUREWITZ, AND H. SHAKED, Acta Crystallogr. Sect. A 34, 662 (1978).
18. N. NIIZEKI AND M. WACHI, Z. Kristallogr. 127, 173 (1968).
19. A. G. TUTOV, I. E. MYL'NIKOVA, N. N. PARFENOVA, V. A. BOKOV, AND S. A. KIZHAEV, Sov. Phys. Solid State 6, 963 (1964).
20. H. MÜLLER-BUSCHBAUM AND D. C. DE BEAULIEU, Z. Naturforsch. B 33, 669 (1978).
21. J. P. REMEIKA, J. Appl. Phys. 31, 263S (1960).
22. S. C. ABRAHAMS AND J. M. REDDY, Phys. Rev. Lett. 13, 688 (1964).
23. S. C. ABRAHAMS, J. M. REDDY, AND J. L. BERNSTEIN, J. Chem. Phys. 42, 3957 (1965).
24. G. T. RADO, Phys. Rev. Lett. 13, 335 (1964).
25. D. T. CROMER AND J. T. WABER, in "International Tables for X-ray Crystallography," Table 2.2A, The Kynoch Press, Birmingham, England (1974).
26. N. WALKER AND D. STUART, Acta Crystallogr. Sect. A 39, 158 (1983).
27. P. N. SWEPSTON, Molecular Structure Corporation (1985).
28. C. J. GILMORE, J. Appl. Crystallogr. 17, 42 (1984).
29. D.T. CROMER AND J. T. WABER, in "International Tables for X-ray Crystallography," Table 2.3.1, The Kynoch Press, Birmingham, England (1974).
30. R. L. CARLIN, "Magnetochemistry," Springer-Verlag, Berlin (1986).
31. M. E. FISHER, Philos. Mag. 7, 1731 (1962).
32. L. J. DE JONGH AND A. R. MIEDEMA, Adv. Phys. 23, 1 (1974).
33. P. C. M. GUBBENS AND A. M. VAN DER KRAAN, J. Less-Common Met. 163, 165 (1990).
34. C. J. M. DENISSEN, B. D. DE MOOIJ, AND K. H. J. BUSCHOW, J. Less-Common Met. 142, 195 (1988).
35. E. V. SINITSYN, O. NIKOLOV, T. TOMOV, T. RUSKOV, AND S. I. IVANOV, Sov. Phys. Solid State 29, 573 (1987).
36. J. L. DORMANN AND M. NOGUES, J. Phys.: Condens. Matter 2, 1223 (1990).
37. F. SCHOLL AND K. BINDER, Z. Phys. B 39, 239 (1980).
38. S. GOSHEN, D. MUKAMEI, AND H. SHAKED, J. Appl. Phys. 40, 1590 (1969).